Physical processes explaining the second force peak generated during a surge impact on a vertical wall

Mohamed Rozki, Stéphane Abadie, Denis Morichon

Coastal Engineering 197 (2025) 104664

Contents lists available at ScienceDirect

Coastal Engineering

journal homepage: www.elsevier.com/locate/coastaleng

Physical processes explaining the second force peak generated during a surge impact on a vertical wall

Mohamed Rozki *, Stéphane Abadie, Denis Morichon

Université de Pau et des Pays de L'Adour, E2S UPPA, SIAME, Anglet, 64600, France

ARTICLE INFO

Keywords:
Tsunami impact
Swash impact
Wave impact
Dam break
Air pocket
OpenFoam
Compressible

ABSTRACT

This paper presents an in-depth study of the impact of a surge on a vertical wall using incompressible and compressible RANS model simulations of a classical dam break experiment over a dry bed. The model allows access to the detailed flow structure and pressure field at any instant, which provides valuable complementary information to measurements. Our study focuses on the second force peak, which is often the largest one and for which the literature does not really provide a clear explanation. Before and after this peak, the pressure on the wall is governed by the flow kinematics in the area. Before the peak, an overpressure appears at the root of the reflected jet, corresponding to the violent interaction between the incoming surge and the run-down flow. At the peak instant, the situation suddenly changes, due to the collapse of the reflected jet onto the incoming flow, trapping an air cavity. As in the classical case of direct wave impact on a wall with a trapped air pocket, this process generates an additional strong uniform pressure field in the air cavity, which propagates to the water and nearby boundaries due to the water confinement effect. This compressible effect, which varies depending on the capacity of air to escape the cavity, explains the formation of the second force peak. Finally, the 3D incompressible model provides a much more reliable estimate of the second force peak than the 2D incompressible model. This is likely due to the air escape phenomenon, which occurs when the experimental initial conditions are not perfectly 2D. Although it is unlikely that the 3D simulation perfectly reproduces the experimental flow, nevertheless, with more or less comparable air escape, the computation results appear consistent.

1. Introduction

Surge impact on a vertical wall is observed in various situations such as tsunami surge (Cross, 1967), overtopped flows (Streicher et al., 2018), flash floods for instance due to a dam break or a levee breach (Kankanamge et al., 2020), interacting with the existing structures or buildings. As such structures have to resist to these extreme flows, an accurate estimation of the force generated is required.

Cross (1967) was among the first to study this problem. Using the previous work of Cumberbatch (1960) on the water wedge impact as a basis, he proposed a formula for the force estimation which he confronted to his experimental data. These two pioneering works reveal interesting features of the problem. First, the incoming momentum of the flow is obviously an important parameter. But, second, the free surface contribution should not be forgotten, hence the introduction of the angle of the surge tip in the formula. The water wedge impact indeed produces much larger pressures when this angle is steep. Accordingly, the formula developed by Cross (1967) focused on the surge tip impact process. This first impulsive impact has then been studied extensively in the literature. The authors have shown that the pressure is heterogeneously distributed over the wall with the peak being at the bottom and the magnitude decreasing upward (Shen et al., 2020; Liu et al., 2022).

Nevertheless, Cross (1967) also noticed that the force peak is actually not associated to this phase of the flow. "As the surge strikes the wall, a considerable amount of water is deflected upwards. The peak of the force record was seen to coincide with the collapse of this deflected column back onto the surge". His formula failed in predicting this force peak magnitude.

Later, experimentally studying bores and surge impact, Ramsden (1996) measured forces signal also clearly depicting two distinct phases, the maximum force occurring again after the impulsive impact phase, during the reflection phase of the flow. Ramsden (1996) also highlighted that the force deduced from the maximum run-up of the flow on the wall, assuming hydrostatic pressure distribution, was always larger than the maximum measured force. He attributed this to the contribution of the vertical flow acceleration.

* Corresponding author.
E-mail addresses: mohamed.rozki@univ-pau.fr (M. Rozki), stephane.abadie@univ-pau.fr (S. Abadie), denis.morichon@univ-pau.fr (D. Morichon).

https://doi.org/10.1016/j.coastaleng.2024.104664
Received 28 August 2024; Received in revised form 7 November 2024; Accepted 26 November 2024
Available online 2 December 2024

In their large scale experiment on bore impact on a vertical wall, Kihara et al. (2015) observed significant uniform pressure exerted over a relatively large portion of the wall during the later stage of the reflection phase. For them, the most likely cause of this pressure pattern was the ultimate collapse of the water column but the exact processes remained unclear (as indicated at the end of their paper). A more heterogeneous pressure field was then generated, which the authors explained by the change of the flow direction near the wall with the incident bore flow rotating counter-clockwise, leading to a roller, and the generation of a secondary flow confined in the corner of the wall rotating clockwise. This particular flow pattern was later clearly confirmed in Tan et al. (2023).

The impact loads on vertical structures were also investigated for irregular waves in large scale experiments. For instance, Streicher et al. (2018) and Streicher et al. (2019) studied storm waves overtopping a dike crest and their impact on a dike mounted vertical wall. They showed that, in this case, the force signal shows similarities to that observed during the impact of tsunami bores with a two peak force pattern. During the second peak, often the largest, the pressure distribution was close to hydrostatic but with a higher slope. They defined this impact type as "quasi static impact", "quasi" referring to a dynamic component attributed to the downward acceleration in the run down. In Ko and Yeh (2018), the maximum impact force also occurred during the down-rush of water in the reflection phase. In this experimental study, the pressure was observed to be uniform during the upward splash up motion and the gradient remained weak during the run-down.

Shen et al. (2020) studied experimentally the spatial and temporal characteristics of the forces generated by a dam-break surge on a vertical wall. Three impact stages were identified: the initial impact, the reflected stage and a second impact stage corresponding to a back bore impact. The maximum force occurred during the reflected stage and was concomitant with the impact of the reflected plunging breaking onto the initial surge as in Cross (1967). During this force peak, the pressure was shown to be uniform in the bottom impact zone. Oscillations of the pressure signal were reported (identical at each elevations) which main frequency corresponded to previous estimations given in Topliss et al. (1993) for an air pocket trapped within water.

Finally, the spatial extent of the uniform pressure associated to the second force peak is somehow highlighted in Huo and Liu (2023). Measuring the pressure field on the wall and on the bottom, the authors showed that the uniform pressure increases observed when the recurved splash-up fall onto the incoming flow also spreads over significant distance over the bottom.

As highlighted in the previous literature review, the second force peak is concomitant with the closure of the deflected flow onto the incoming surge and the associated pressure distribution seems to be quite uniform and spatially extended. Nevertheless, despite this knowledge, the physical reasons explaining this second force peak are still unclear.

The present study investigates the process behind the generation of this second force peak occurring during surge impacts. Our hypothesis is that the overall pressure increase leading to this peak results from a piston effect caused by the closure of the water lip over the air volume. This assumption is further explored in the following sections with Reynolds Averaged Navier–Stokes (RANS) simulations based on the incompressible model *interFoam* (in 2D and 3D) and the compressible model *compressibleInterFoam* from OpenFOAM. The study by Lobovský et al. (2014) provides valuable experimental data for the impact of a surge wave, generated by a dry dam break, on a vertical wall. This study gives access to the results of a series of repeated experiments including detailed pressure data, accurate water height measurements, and clear snapshots of the water–air interface allowing for thorough analysis of the impact physics. In this paper, this data set is used as a reference to guide the interpretation of our simulation results. The experiment studied in Lobovský et al. (2014) is simulated with an incompressible model in 3D and in 2D. A compressible simulation in 2D is also carried out to complete the interpretation.

The paper is structured as follows. After this introduction, Section 2 presents the models used and the benchmark case. Section 3 shows the results which are discussed in Section 4. Finally, the last section presents the conclusions of the study.

2. Methodology

2.1. Presentation of the numerical models

In this study, the unsteady multiphase Reynolds-Averaged Navier–Stokes (RANS) Equations are solved to simulate the water and air flow. For this purpose, two-phase Navier–Stokes solvers from OpenFOAM are employed: one incompressible, *interFoam*, and the second one, compressible, namely, *compressibleInterFoam*. Both are based on the finite volume method coupled with the Volume Of Fluid (VOF) algorithm to simulate the flow of two non-miscible phases.

2.1.1. InterFoam

In the incompressible model *interFoam*, the continuity and momentum equations read respectively:

$$\nabla \cdot \mathbf{u} = 0 \tag{1}$$

$$\frac{\partial \rho \mathbf{u}}{\partial t} + \nabla \cdot (\rho \mathbf{u}\mathbf{u}) = -\nabla p + \nabla \cdot (2(\mu + \mu_t)\mathbf{D}) + \rho \mathbf{g} + \sigma \kappa \nabla \alpha \tag{2}$$

In which, ρ represents the fluid density, $\mathbf{u}$, the velocity vector at the cell center, p the pressure, $\mathbf{g}$ the gravitational acceleration vector, μ and μ_t the dynamic and turbulent viscosity, respectively, $\mathbf{D} = \frac{1}{2}(\nabla \mathbf{u} + (\nabla \mathbf{u})^T)$ the strain rate tensor and σ the surface tension coefficient relative to the two phases solved. The average curvature of the interface, κ, is estimated by $\nabla \cdot (\nabla \alpha / |\nabla \alpha|)$, where α is the water volume fraction, defined as:

$$\alpha(x,t) = \begin{cases} 1 & \text{if water is present at } x,t \\ 0 & \text{else.} \end{cases} \tag{3}$$

These equations are supplemented by the water phase advection equation given by:

$$\frac{\partial \alpha}{\partial t} + \nabla \cdot (\alpha \mathbf{u}) = 0 \tag{4}$$

Due to the discontinuity of α at the interface, solving this pure advection equation without an adapted method leads to the smearing of the interface and the unboundedness of the solution. Here, we employed the Interface Compression method described in Okagaki et al. (2021). This method consists in adding an artificial compression term to the equation which allows to keep the interface sharp. The user defines a compression coefficient to tune the compression amount. In the present study, this coefficient is equal to 1. 3 is then discretized with the finite volume method and solved with the Multidimensional Universal Limiter for Explicit Solution (MULES) method, which maintains the boundedness of the phase fraction (Deshpande et al., 2012).

The local fluid properties are then averaged in a computational cell following:

$$\rho(x,t) = \alpha(x,t)\ \rho_w + (1 - \alpha(x,t))\ \rho_a \quad \mu(x,t) = \alpha(x,t)\ \mu_w + (1 - \alpha(x,t))\ \mu_a \tag{5}$$

with ρ_w and ρ_a, the water and air density, and μ_w and μ_a, the water and air viscosity.

To model the turbulence, the standard $k - \epsilon$ model is used in this study. In the latter, the turbulent viscosity is expressed as $\mu_t = \rho\, C_\mu \frac{k^2}{\epsilon}$. The governing equations for the turbulent kinetic energy k and the rate of dissipation of turbulent kinetic energy ϵ are respectively given by:

$$\frac{\partial \rho\, k}{\partial t} + \nabla \cdot (\rho\, k\, \mathbf{u}) = \nabla \cdot \left(\left(\frac{\mu_t}{\sigma_k} + \mu \right) \nabla k \right) + P_k - \rho \epsilon, \tag{6}$$

$$\frac{\partial \rho\, \epsilon}{\partial t} + \nabla \cdot (\rho\, \epsilon\, \mathbf{u}) = \nabla \cdot \left(\left(\frac{\mu_t}{\sigma_\epsilon} + \mu \right) \nabla \epsilon \right) + \frac{C_{1\epsilon}\, \epsilon}{k} P_k - \frac{\rho\, C_{2\epsilon}\, \epsilon^2}{k}. \tag{7}$$

Where $P_k = 2\mu_t D_{ij} D_{ij}$ is the production of turbulent energy and C_μ, σ_k, σ_ϵ, $C_{1\epsilon}$, $C_{2\epsilon}$ are constants values respectively equal to 0.09, 1.0, 1.3, 1.44, 1.92.

2.1.2. CompressibleInterFoam

In the compressible solver *compressibleInterFoam*, Eqs. (2), 3, (4), (5), (6), (7) are solved similarly as in *interFoam*. The differences concern the mass and energy conservation equations.

The mass conservation now reads:

$$\frac{\partial \rho}{\partial t} + \nabla \cdot (\rho \mathbf{u}) = 0 \tag{8}$$

The energy conservation is here expressed in function of the temperature T (as $e = c_v T$ with e the internal energy and c_v the heat capacity at constant volume):

$$\frac{\partial \rho T}{\partial t} + \nabla \cdot (\rho T \mathbf{U}) = \nabla \cdot (\mu_{\text{th}} \nabla T) - \left(\frac{\alpha_{\text{water}}}{c_{v,\text{water}}} + \frac{1 - \alpha_{\text{water}}}{c_{v,\text{air}}} \right) \times \left(\frac{\partial \rho K}{\partial t} + \nabla \cdot (\rho K \mathbf{U}) + \nabla \cdot (p \mathbf{U}) \right) \tag{9}$$

With $K = \frac{|\mathbf{U}|^2}{2}$ the specific kinetic energy, μ_{th} the thermal diffusivity and $c_{v,\text{water}}$ and $c_{v,\text{air}}$, the specific heat capacities at constant volume for the water and air phases, respectively.

The closure of the system requires an equation of state for the density ρ. The state equations and constants for air and water are the same as those used in the study by Ma et al. (2016).

Air is considered as a perfect gas. Therefore, the density of air is linked to the pressure and the temperature by the equation:

$$p R_{air} T = \rho_{air} \tag{10}$$

where $R_{air} = 287\,\text{J/kg K}$ is the specific gas constant.

Water is treated as a barotropic fluid with this equation:

$$\rho_{water} = \rho_{0,water} + \psi (p - p_0) \tag{11}$$

where $\rho_{0,water}$ is the initial density at the initial pressure p_0, and $\psi = \frac{1}{R_{water} T}$ is the compressibility coefficient. In this work, $R_{water} = 3000\,\text{J/kg K}$ is used.

A validation of this model in a 1D piston problem is proposed in Appendix. The model used here is the same as the one presented in Ma et al. (2016). In the later study, *compressibleInterFoam* was validated against the experimental data of Lugni et al. (2010b), featuring a wave impact on a wall with a trapped air pocket.

2.2. Benchmark case

2.2.1. Experimental configuration

In this paper, the dam break flow studied experimentally in Lobovský et al. (2014) is simulated. The channel used in this experiment was 1.61 m long, 0.6 m high and 0.15 m wide. The upstream reservoir, which spans a length of 60 cm from the upstream end of the channel, was filled with water to a depth of 30 cm. Pressure sensors, numbered in ascending order from the bottom to the top, recorded the pressure evolution at different heights (3 mm, 15 mm, 30 mm, and 80 mm) along the central axis of the wall. An additional off-center sensor was used to measure the lateral pressure variations and assess the three-dimensionality of the flow. The sampling frequency of these sensors was set to 20 kHz.

Fig. 1 shows the sketch of the case simulated. Note that in the simulation, the height of the domain has been extended to 0.8 m to allow for the run-up generated by the surge on the downstream vertical wall, slightly larger the height of the channel in the experiment, to be properly resolved.

In the analysis of the results, the force on the vertical wall is estimated by integrating the discrete pressure measurements using the trapezoidal integration method. When the numerical results are compared with the experiment of Lobovský et al. (2014), the force is only calculated over the portion of the wall equipped with sensors. In this case, the force calculated is named F_{Lob}. The total force on the wall is also calculated in the paper and is named F_{wall}.

2.2.2. Models settings

Table 1 presents the settings of the two models used for the simulations of this study case according to the nomenclature used in OpenFOAM (the reader is referred to the model user manual for the detailed signification of these keywords).

As stated in this table, in *interFoam* and *compressibleInterFoam*, the time step is dynamically adjusted based on the CFL, which values are given in Table 1. In the pressure plots presented in this paper, the pressure is sampled at a time varying frequency corresponding to the instantaneous computational time step. Around the first force peak (i.e., over a time window of about two rise time duration), the average frequency is about 2 kHz for each model (i.e., the incompressible 2D and 3D models and the compressible 2D model). Around the second force peak, this value rises to about 4.5 kHz for the incompressible models and 2.7 kHz for the compressible model. As previously indicated, in the experiment, the acquisition frequency was 20 kHz which is a higher value. Nevertheless, as the CFL condition allows to prevent brutal changes in the flow during the simulation, it also indirectly allows to correctly follow the impact process by adjusting the time step when required. Therefore, the indicated frequencies are sufficient to obtain a relevant pressure signal.

Several sensitivity tests were conducted to assess the model performance. Table 1 displays the selected model configurations for the incompressible model and the compressible model, referred to model 1 and model 2 respectively. Regarding the turbulence initial values, different turbulence intensities I were tested (with $k = \frac{3}{2}(U_0 I)^2$ and U_0 a characteristic velocity, here the surge velocity equal to 3 m/s from Lobovský et al. (2014)), following the methodology described in Park et al. (2012). For turbulence intensities up to 5%, the model results match the data reasonably well, while for larger intensities, a larger discrepancy is noted especially regarding the arrival time of the surge front compared to the experiment. Therefore, small initial values for k and ϵ were used (i.e., 10^{-4} associated to the corresponding units), which is coherent with a flow initially at rest and in line with the recent study of Iphineni et al. (2024). Regarding the cell size in the three directions, the values presented in Table 1 allow to obtain a good correspondence (not the optimal one) with the experimental data while maintaining the computational time within reasonable bounds. A mesh sensitivity study was also conducted, considering larger and smaller cell sizes than the one finally retained. This study showed that there are some variations of the results with the mesh size but overall the pressure signals look similar while matching more or less accurately the data. As usually observed with this type of models (i.e., RANS - VOF), there is no formal convergence of the results while refining the mesh. The reason is that while reducing the cell size, the model starts capturing very fine scale processes, like complex 3D interface fragmentation or the inclusion of small air bubbles, but the cell size is not small enough or the correct physics not really included to really resolve these features. Nevertheless, the impact pressure, for instance, is dependent on these small flow characteristics and is therefore varying accordingly. Overall, the model should be able to capture the macroscale physics of the problem with a reasonable resolution, while being unable to solve at the same time the microscale processes. Therefore, our approach is to reduce the appearance of these small scale features by using an intermediate mesh resolution.

3. Results

3.1. Incompressible computation

The results obtained with the incompressible model (*interFoam*) in 2D and 3D are presented first.

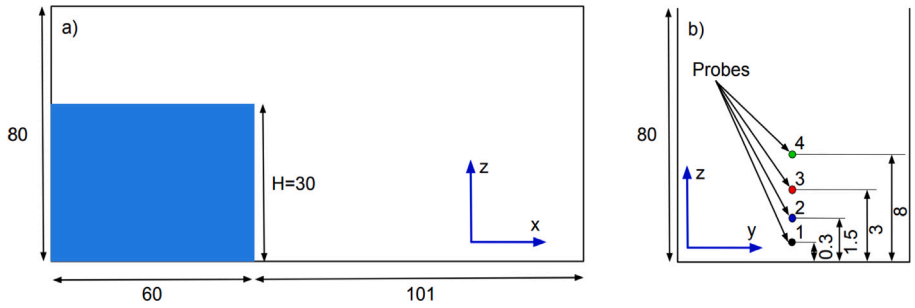

Fig. 1. Sketch of the case simulated which corresponds to the experimental study described in Lobovský et al. (2014)(a) and position of the pressure sensors (b). The dimensions, represented with a distorted scale, are in cm.

Table 1
Setup of the two models used to simulate the dam break flow of Lobovský et al. (2014).

Model 1: Lobovský et al. (2014) simulated with *interFoam*					
Mesh Size	$\Delta x = \Delta z = 0.004$ m, $\Delta y = 0.01$ m in 3D and $\Delta y = 0.15$ m in 2D				
CFL	$CFL_{max} = 1$ (maxCo)				
Initial conditions	**alpha.water**	**epsilon** (m^2/s^3)	**k** (m^2/s^2)	**p_rgh** (Pa)	U (m/s)
Initial Values	as in Fig. 1(a)	10^{-4}	10^{-4}	0	(0 0 0)
Boundary	**alpha.water**	**epsilon** (m^2/s^3)	**k** (m^2/s^2)	**p_rgh** (Pa)	U (m/s)
Walls	zeroGradient	epsilonWallFunction	kqRWallFunction	fixedFluxPressure	noSlip
Atmosphere	inletOutlet	inletOutlet	inletOutlet	totalPressure	pressureInletOutletVelocity
Model 2: Lobovský et al. (2014) simulated with *compressibleInterFoam*					
Mesh Size	$\Delta x = \Delta y = 0.004$ m, $\Delta z = 0.15$ m				
CFL	$CFL_{max} = 0.5$ (maxCo)				
Initial conditions	**alpha.water**	**epsilon** (m^2/s^3)	**k** (m^2/s^2)	**p_rgh** (Pa)	U (m/s)
Initial Values	as in Fig. 1(a)	10^{-4}	10^{-4}	10^5	(0 0 0)
Boundary	**alpha.water**	**epsilon** (m^2/s^3)	**k** (m^2/s^2)	**p_rgh** (Pa)	U (m/s)
Walls	zeroGradient	epsilonWallFunction	kqRWallFunction	fixedFluxPressure	noSlip
Atmosphere	inletOutlet	inletOutlet	inletOutlet	totalPressure	pressureInletOutletVelocity

3.1.1. Snapshots of free surfaces

The snapshots of the numerical simulations are compared with the experimental data of Lobovský et al. (2014) in Fig. 2 (panels a1 to f1). The time is expressed in adimensional form with $t^* = \frac{t}{\sqrt{H/g}}$. This figure first illustrates the two different phases of the surge impact. The first phase occurs when the surge strikes the base of the wall and ascends (Fig. 2(a1), (b1), (c1)). The second phase corresponds to the reflection of the flow on the wall until it reconnects with the incoming flow (Fig. 2(d1), (e1), (f1)).

The simulations with *interFoam*-3D capture correctly the water–air interface dynamics measured during the first impact stage. Nevertheless, notable differences are observed during the second stage. The run-down occurs in two phases in the experiment. It starts with disorganized 3D collapsing of a fraction of the water located in the vertical column (Fig. 2(c1)), followed by a more organized back breaking jet (Fig. 2(d1)). Only this second stage is correctly reproduced by the model. The result is that, after reconnection, the trapped air cavity is clearly made up of a mix of air and water, while it is only composed of air in the simulation (Fig. 2(e1)). These differences are understandable as the experiment is in part the result of the gate-lift motion and channel imperfections which are not replicated in the idealized simulations.

If the results obtained from the 3D and the 2D models are undistinguishable in the first phase of the flow (Fig. 2 (a1) to (c1)), differences start to appear during the reflection stage (Fig. 2 (d1) to (f1)). In 2D, the jet is reflected a little farther away from the wall and as a result, the air cavity is sightly larger (Fig. 2 (e1)).

The streamlines calculated with the 3D model and presented in Fig. 2 (panels (a2) to (f2)), illustrate the complexity of the flow during the reflection stage with multiple recirculations. The internal flow structure will be analyzed in further details in Section 3.1.4.

3.1.2. Pressure signals

The pressure signals along the wall obtained from both 2D and 3D simulations are compared with the data in Fig. 3. The two impact phases identified previously in Fig. 2 have distinct pressure patterns. The first impact leads to a strong initial peak at the base of the wall (probe 1) around $t^* = 2.5$, which diminishes in intensity as it moves up the wall (probe 2, 3 and 4). The second stage corresponding to the air cavity entrapment around $t^* = 6$ is associated to a lower but more uniform peak, as it is observed with a similar intensity at each probe.

The two simulations reproduce the overall evolution of the pressure signal measured by the 4 probes. The rise time of the pressure during the initial impact phase is reasonably well captured in 2D and 3D even though the decrease of the pressure peak with the height is larger in the simulations. The errors on the first pressure peak assessment are the following for *interFoam*-2D and *interFoam*-3D, respectively: 3.52% and 27.80% at probe 1, 1.90% and 7.13% at probe 2, 18.91% and 15.58% at probe 3 (no peak at probe 4). There are also notable differences, especially for the 2D model, on the pressure plateau following the first peak between $t^* = 3$ and $t^* = 5.5$.

The most striking difference between observations and computations is noted at the time of the air cavity closure around $t^* = 6$. Here, the second pressure peak calculated with *interFoam*-2D drastically exceeds the data while the one calculated with *interFoam*-3D reproduces

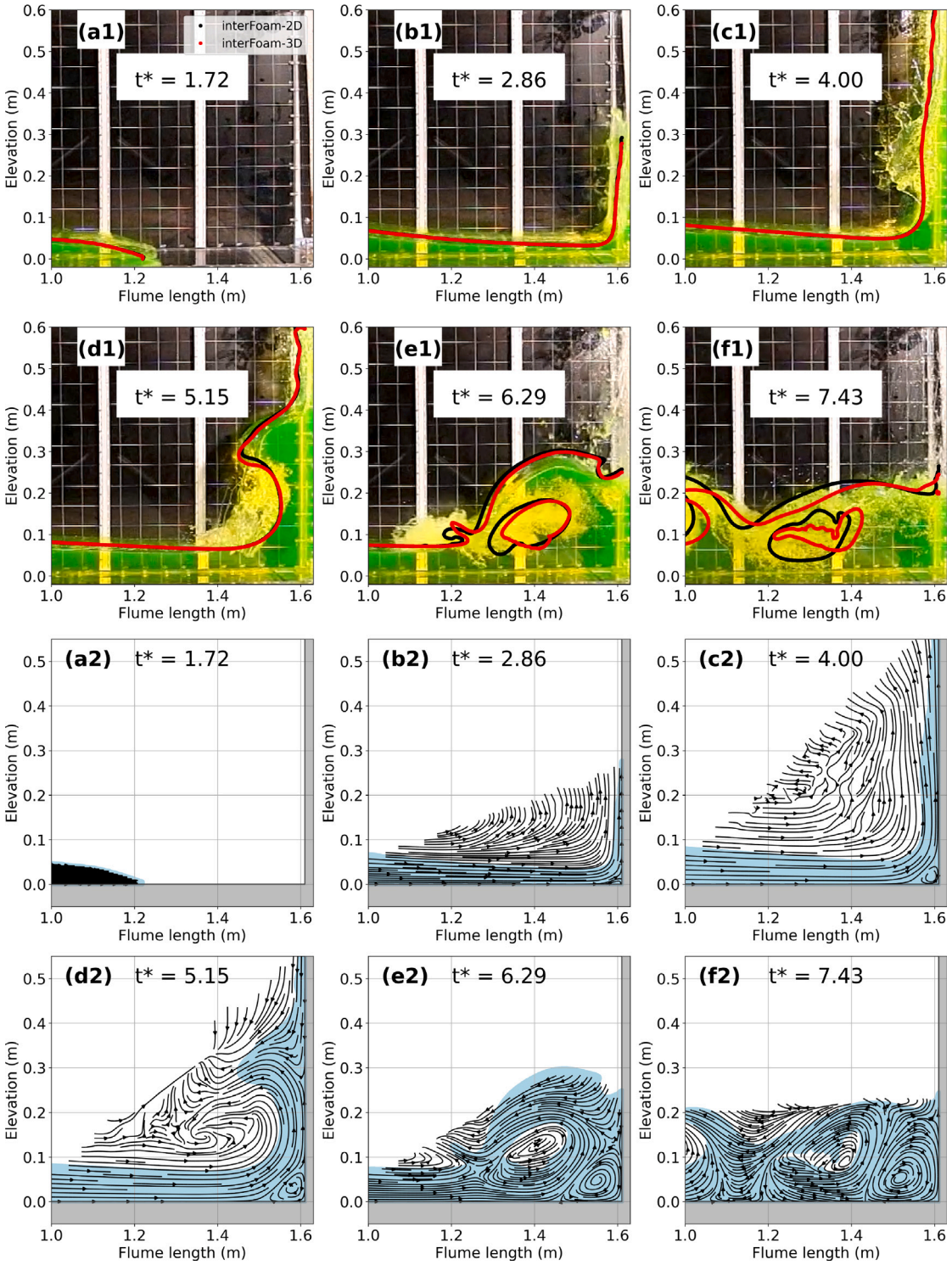

Fig. 2. Panels (a1) to (f1): Successive snapshots of the water flow measured in Lobovský et al. (2014) and the corresponding free surfaces calculated by the incompressible model *interFoam* in 2D (black line) and in 3D at the central cross-section $y = 0$ (red line). Panels (a2) to (f2): water volume fraction and streamlines at the same instants for the 3D model taken at the central cross-section $y = 0$. $t^* = \frac{t}{\sqrt{H/g}}$.

this phase much better. On the second pressure peak, the errors are the following for *interFoam*-2D and *interFoam*-3D, respectively: 108.51%, 8.71% at probe 1, 109.52%, 3.05% at probe 2, 118.38%, 2.90% at probe 3, 131.87%, 7.94% at probe 4. The large error observed with *interFoam*-2D is explained in Sections 3.2 and 3.1.5.

3.1.3. Evolution of the impact force

Fig. 4 shows the comparison between the data and the simulations performed with the two incompressible models regarding the variable F_{Lob}. This figure shows two interesting results. First, the behavior of both models is the same for the first peak while differing strongly for

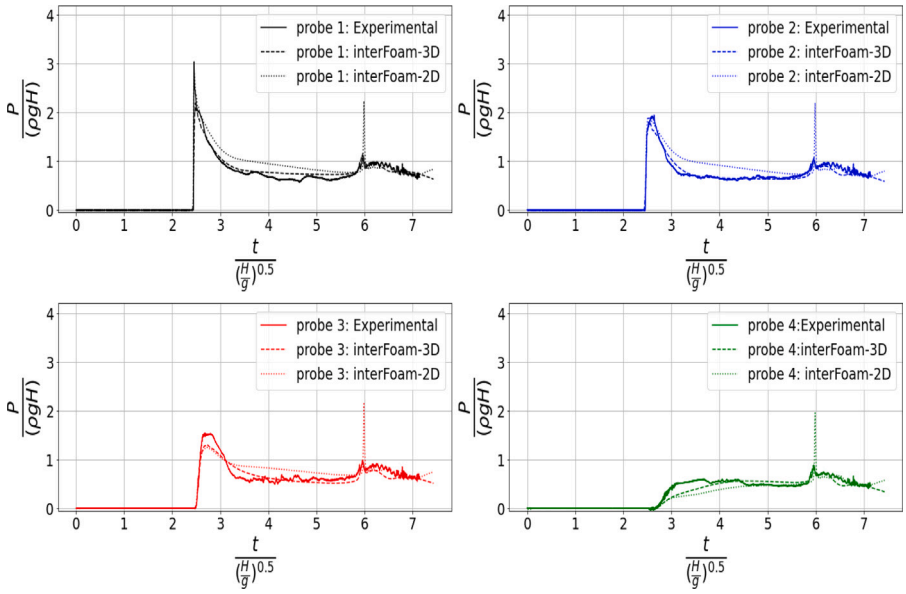

Fig. 3. Comparison between the computed pressure and the data at the probes position of Lobovský et al. (2014).

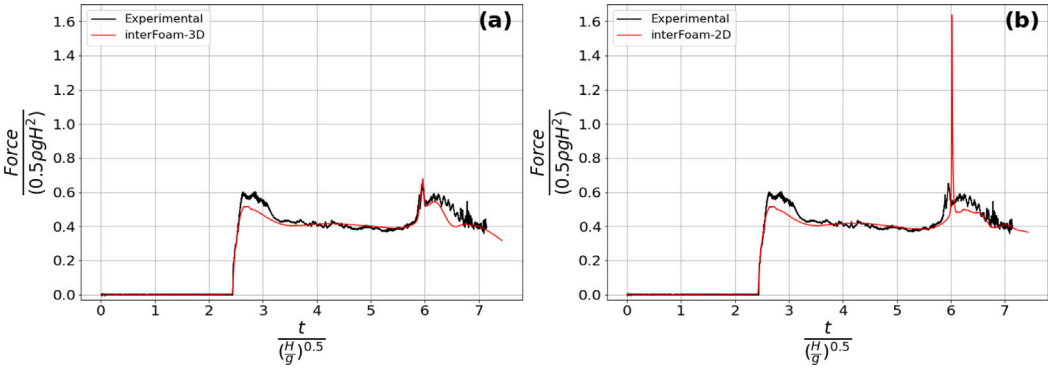

Fig. 4. Comparison between the experimental (Lobovský et al., 2014) and the computed (*interFoam*-3D: (a), *interFoam*-2D: (b)) forces on the bottom part of the wall F_{Lob}.

the second force peak. The correspondence with the data is correct for the first peak, with a slight underestimation of the models, and satisfactory for the second peak for the 3D model. Conversely, with *interFoam*-2D, the error of the model at $t^* = 6$ is 253%.

Fig. 5 shows the evolution of the global impact force F_{wall} calculated with the two incompressible models. The equivalent hydrostatic force has been added to this plot. The latter is computed with the instantaneous water level on the wall considering an hydrostatic pressure distribution.

This figure reveals several interesting results. The decrease of the force observed after the first force peak in F_{Lob} is no longer present in F_{wall}. Instead, the global force on the wall just slightly decreases around $t^* = 3.5$ before starting a gradual ascent toward the second peak. Just before $t^* = 6$, there is a clear break in the slope of the curve. Around $t^* = 6$, F_{wall} increases drastically to reach the peak value which strongly differs between the two models. Now, the ratio between the second and the first peak is large, unlike in the case of F_{Lob} where both peaks were equivalent (this ratio is about 3 for the 3D model and about 7 for the 2D model). After the peak, the two models start again to behave similarly.

The comparison with the equivalent hydrostatic force is very instructive. F_{wall} appears very different from the hydrostatic equivalent. The red curve shows that the run-up and run-down phases occur between $t^* = 2.5$ and $t^* = 6.5$, with the maximum run-up reached at $t^* = 4.5$. F_{wall} is not sensitive to the run-up motion while it starts to increase in phase with the run-down motion. This particular behavior of the force is likely related to the flow acceleration along the wall and calls for an investigation of the flow kinematics.

3.1.4. Internal flow structure

In this section, we study the relationship between the flow and the pressure. All the results presented here correspond to 3D incompressible simulations. The model ability to simulate a realistic flow structure has been validated with respect to the case studied in Tan et al. (2023). The results of this validation are presented in Appendix B of this paper.

In the case studied here, which corresponds to the experiment of Lobovský et al. (2014), the internal flow structure simulated with the 3D model varies only slightly along the lateral direction y as observed on Fig. 6. This explains why 2D and 3D simulations results are almost identical except for a short period around the second force peak (i.e., $t^* \approx 6$) (Fig. 5). Nevertheless, we note that there is a slight variation of the free surface in the different cross sections of Fig. 6. This variation is important during the second force peak stage as will be shown later in the paper.

Fig. 7 shows the evolution of the vertical pressure distribution and the internal flow structure along the wall during the run-up and run-down phases. During the run-up of the jet, (Fig. 7, panels (a) to (c)), the flow is essentially characterized by a violent change in direction of the main flow from the horizontal to the vertical direction. On the lower corner, a recirculation zone starts appearing. The pressure is very high at the bottom of the wall due to the impulsive impact of the surge front

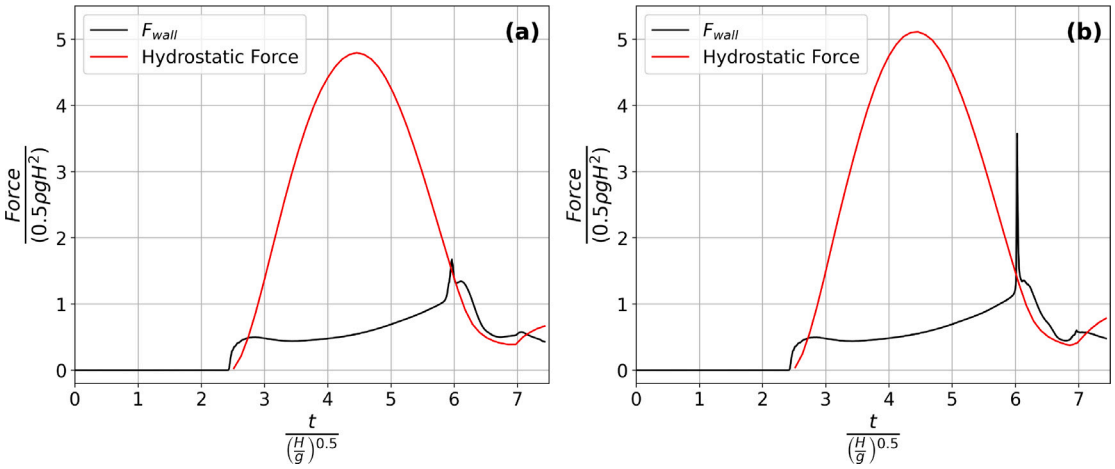

Fig. 5. Time evolution of the global force F_{wall} and the equivalent hydrostatic force calculated with the incompressible models. Panel (a): *interFoam*-3D, panel (b): *interFoam*-2D.

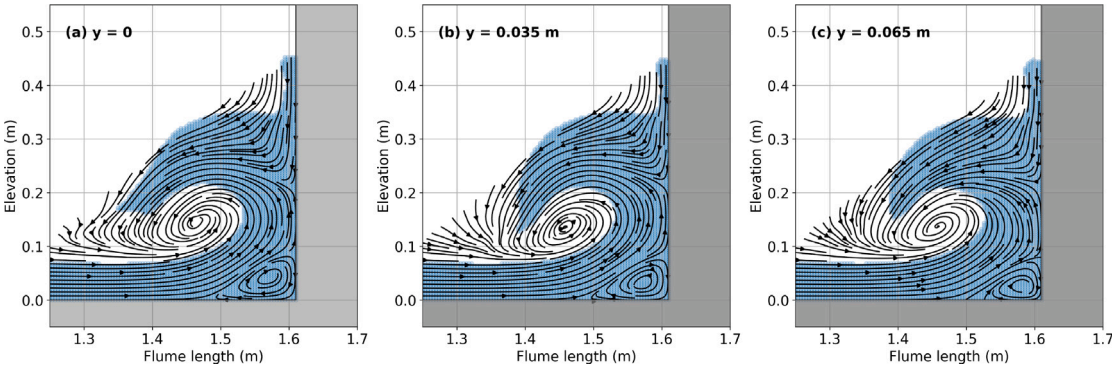

Fig. 6. Flow streamlines and water free surface at $t^* = 5.71$ (with $t^* = \frac{t}{\sqrt{H/g}}$) calculated by *interFoam*-3D in three different cross-sections.

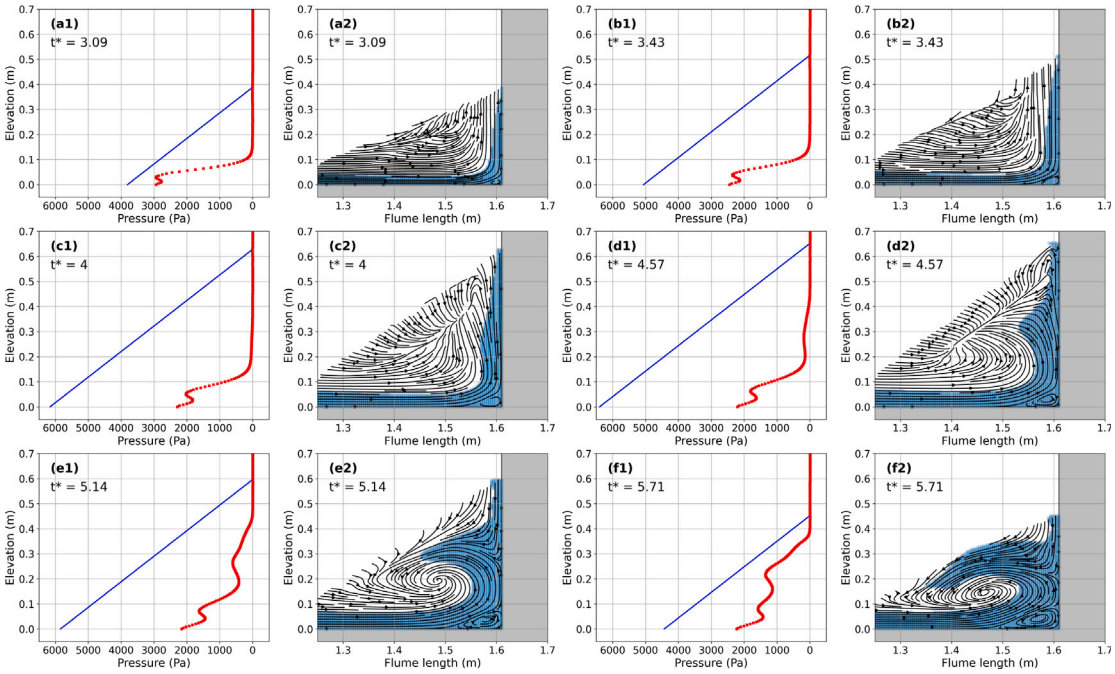

Fig. 7. Flow structure and pressure distribution along the wall calculated by *interFoam*-3D at different times during the run-up and run-down phases. On the pressure profile, the blue line features the equivalent hydrostatic pressure distribution corresponding to the water elevation. $t^* = \frac{t}{\sqrt{H/g}}$.

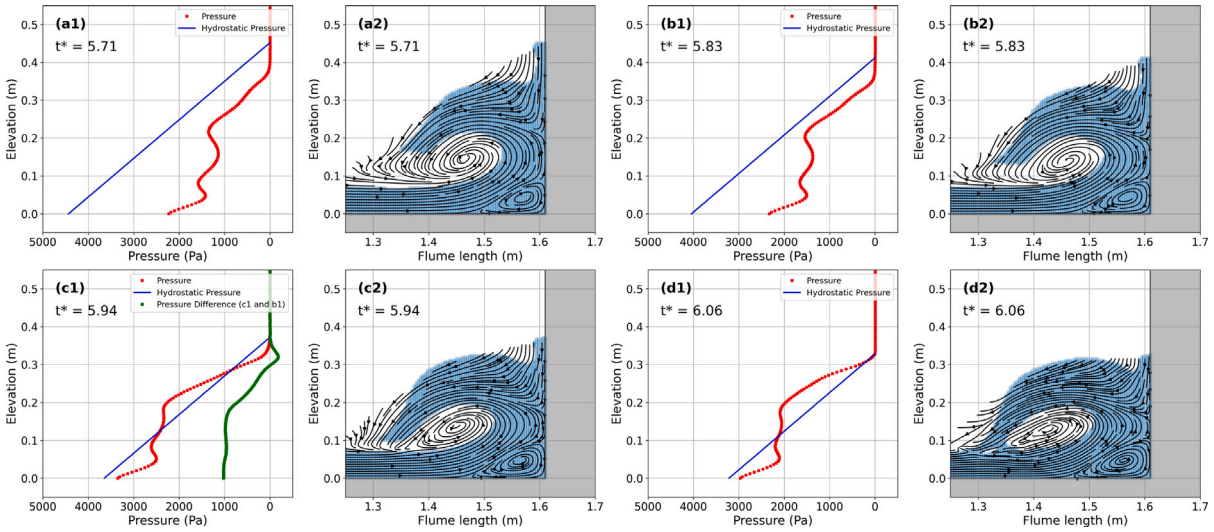

Fig. 8. Flow structure and pressure distribution along the wall calculated by *interFoam*-3D at different times during the air cavity closure. On the pressure profile, the blue line features the equivalent hydrostatic pressure distribution corresponding to the water elevation. $t^* = \frac{t}{\sqrt{H/g}}$.

but decreases very rapidly higher along the wall. In fact, the pressure on the wall is nil in most of the run-up flow (i.e. for $z > 0.1$m) during this stage and the deviation from the hydrostatic distribution (blue line) is striking. This explains why F_{wall} is so different from the hydrostatic force in Fig. 5.

At $t^* = 4.57$, the run-down phase begins. At $t^* = 5.14$, the run-down volume interacts with the upcoming surge flow forcing it to reflect from the wall. Actually, at this stage, both the upcoming surge and the run-down flows, are forced to change their directions which progressively forms the reflected jet. The violent interaction of these two water masses explains the increase of pressure observed on the wall and the increase of the force F_{wall} before $t^* = 6$.

These conditions change drastically at the time of the cavity closure (Fig. 8(c1)). At this time (i.e., $t^* = 5.94$), there is a sudden increase of the pressure on the wall. This increase is very brief as it is no longer present at $t^* = 6.06$. The difference between the pressure at $t^* = 5.94$ and $t^* = 6.06$ shows that the increase is more or less uniform over the first 15 cm of the wall and then lower progressively to 0 over the next 15 cm.

3.1.5. Comparison between 2D and 3D incompressible computations

The significant difference observed between the intensity of the second peaks whether in pressure (Fig. 3) or in force (Fig. 4) computed with the 2D and 3D incompressible models, finds an explanation in Fig. 9. This figure displays the water–air interface at the moment of air cavity entrapment for the two computations. The clear difference which emerges between the *interFoam*-2D and *interFoam*-3D calculations is the capacity of air to escape or not from the cavity during its closure. In the 2D computation (Fig. 9(a1, b1, c1)), the falling lip is perfectly 2D and consequently, only a small fraction of the air can escape during the closure phase. Conversely, in 3D (Fig. 9(a2, b2, c2), the falling lip is not perfectly bi-dimensional with the central portion being slightly slower. This is explained by an interesting feature of the 3D flow. Before impacting the wall, the central portion of the fluid is actually faster due to the no-slip condition at the lateral boundaries. When impacting the wall, the oblique surge front in the vicinity of the corner induces a flow convergence toward the corner and the flow accelerates in this region. This eventually creates an opening during the closure of the lip, through which air can progressively escape (see Fig. 9(c2)).

3.2. 2D compressible computations

Figs. 3 and 4 showed a drastic increase in the pressure and the force in the 2D incompressible simulation during the closure of the air pocket. This increase is not realistic and is due to the difficulty of the incompressible model to solve this stage of the flow, which in reality involves compressible effects due to the air cavity closure. This is demonstrated in Fig. 10, which shows the time evolution of the air cavity volume after its closure as calculated by the 2D incompressible model. The strong volume decrease observed is obviously incompatible with the incompressible assumption and is due to an imperfect resolution of this stage of the flow by the model.

For this reason, compressible simulations of the Lobovský et al. (2014) test case are performed. In this section, the 2D simulation results are presented, as the most critical scenario with the strongest compressibility effects.

3.2.1. Evolution of the force in 2D

Fig. 11 shows the temporal evolution of the impact forces calculated by the model *compressibleInterFoam*-2D and the comparison with *interFoam*-2D (left panel) and the data (right panel). On the left panel, the two curves coincide until the time of the second peak. At this stage (i.e., between $t^* = 6$ and $t^* = 6.7$), they start to diverge. Conversely to the 2D incompressible simulation, the impact force calculated by *compressibleInterFoam*-2D exhibits oscillations that gradually diminish over time. The main frequency of this part of the force signal, calculated as the inverse of the average of the periods between two oscillations, is found around 37 Hz. Eventually, from $t^* = 6.7$, the force curves calculated by *interFoam* and *compressibleInterFoam* converge again. The comparison with the data (right panel) shows that, as in the case of the 2D incompressible model, the 2D compressible model also overestimates the measurements around the time of the second peak.

3.2.2. Correlation between the force and the air cavity volume

Fig. 12 shows the time evolution on the air cavity volume and the force on the wall around the second peak. The air cavity volume oscillates with a frequency very similar to the force (i.e., ≈ 37 Hz) but in opposite phase. Hence, minimum in the air cavity volume corresponds to maximum in the force and vice versa.

Additionally, the signal of the air pocket volume dampens over time, though not as quickly as observed in the force signal.

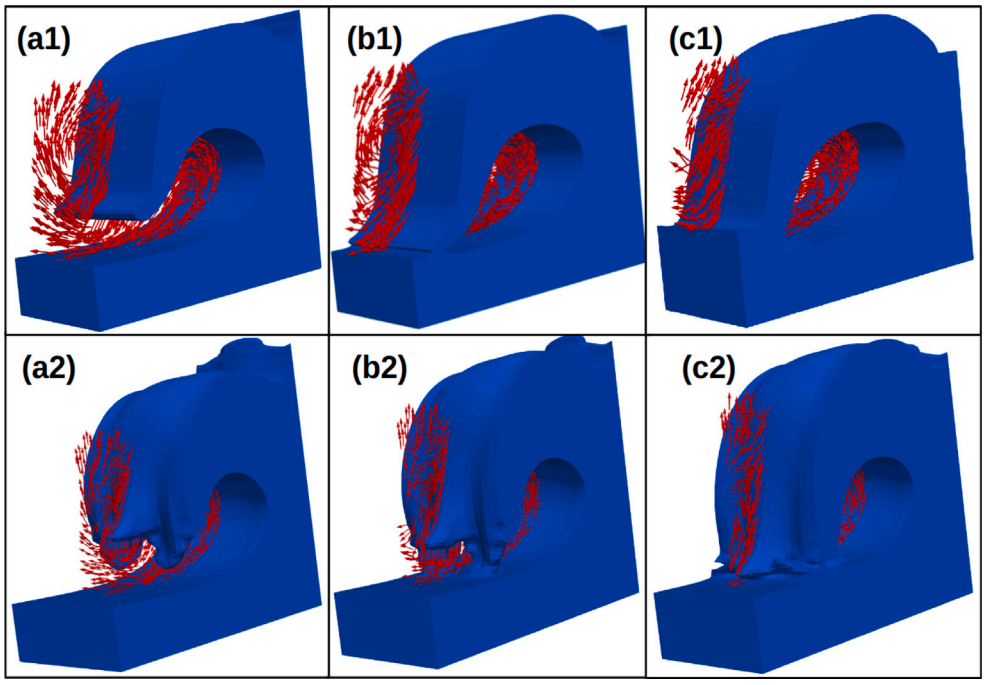

Fig. 9. Snapshots of water/air interfaces and velocity vectors around the cavity computed with *interFoam*-2D (top row) and *interFoam*-3D (bottom row) at instants near the cavity closure. a1: $t^* = 5.98$, b1: $t^* = 6.06$, c1: $t^* = 6.15$; a2: $t^* = 5.83$, b2: $t^* = 5.92$, c2: $t^* = 6.00$, with $t^* = \frac{t}{\sqrt{H/g}}$.

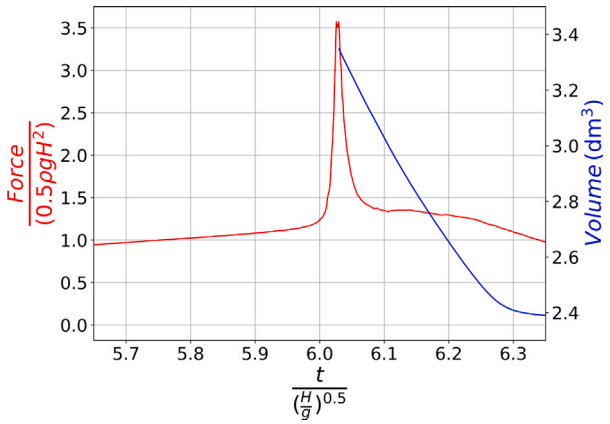

Fig. 10. Evolution of the impact force F_{wall} and the volume of the cavity after its closure calculated by *interFoam*-2D.

3.2.3. Pressure field

Fig. 13 shows the pressure field before the closure of the air pocket ($t^* = 5.48$) and after it, when the force oscillations are significantly damped ($t^* = 6.97$). Before the closure (Fig. 13(a)), the pressure distribution is in line with the pressure profile calculated with *interFoam*-3D in Fig. 8. The maximum pressure is at the bottom. Higher up along the wall, the pressure is more or less constant in the deflection jet zone previously mentioned. Furthermore, the pressure decreases in the higher portion of the water body. Some time after the closure (Fig. 13(b)), the pressure distribution remains unchanged along the wall, while the pressure increases logically in the falling jet reconnection zone.

Between those two moments, Fig. 12 shows that the pattern of the force signal is dominated by the compression and decompression cycles of the trapped air pocket. The corresponding change in the pressure field is investigated through the analysis of Fig. 14. The times of the subplots correspond to the extrema of the air pocket volume marked by black dots in Fig. 12. The process starts with the extreme compression of the air pocket shown in Fig. 14(a). At this time, the pressure is at its highest level in the air pocket. Between the pocket and the wall, the pressure gradually increases reaching its maximum value at the bottom corner of the wall. When the air pocket volume expands to its maximum value (Fig. 14(b)), the pressure in the cavity becomes sub-atmospheric. The pressure on the wall is about P_{atm}, which means that the wall does not feel water anymore. This is associated to the sudden drop of the intensity of the force acting on the wall as observed in Fig. 11 at the same time. It is worth noting the presence of a pressure peak at the lip reconnection point, whether during the compression or decompression phase of the air cavity. This peak is due to the falling water lip striking the incoming surge free surface. For the other compression/decompression cycles, the same patterns are observed but with decreasing relative intensities.

4. Discussion

This paper proposed an in-depth study of the impact of a surge on a vertical wall using incompressible and compressible RANS model simulations of a dambreak over a dry bed similar to the experiment of Lobovský et al. (2014). The model allows to access to the detailed flow structure and to the pressure field at any instant which provides precious complementary information to measurements. Our study focuses on the second force peak which is often the largest one (Cross, 1967; Streicher et al., 2019) and for which, the literature does not really give a clear explanation.

The results presented in this paper covers different aspects of this interesting flow. They are interpreted sequentially in the following sections.

4.1. Pressure and force during the run-up

During the run-up and the run-down of the surge, as already found in previous studies (Ramsden, 1996; Streicher et al., 2018; Ko and Yeh, 2018), the force on the wall was shown to be much lower than the hydrostatic equivalent (Fig. 5). This is due to the particular pressure

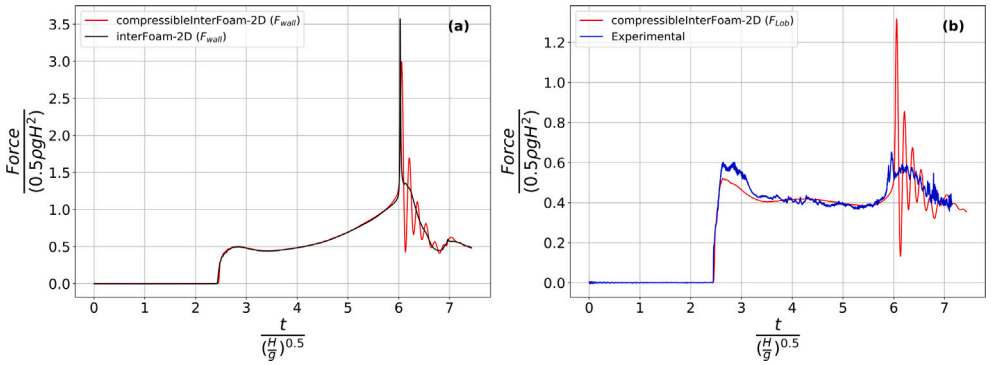

Fig. 11. Impact forces calculated with the *compressibleInterFoam*-2D. Left panel: F_{wall} and comparison with *interFoam*-2D, right panel: F_{Lob} and comparison with the data.

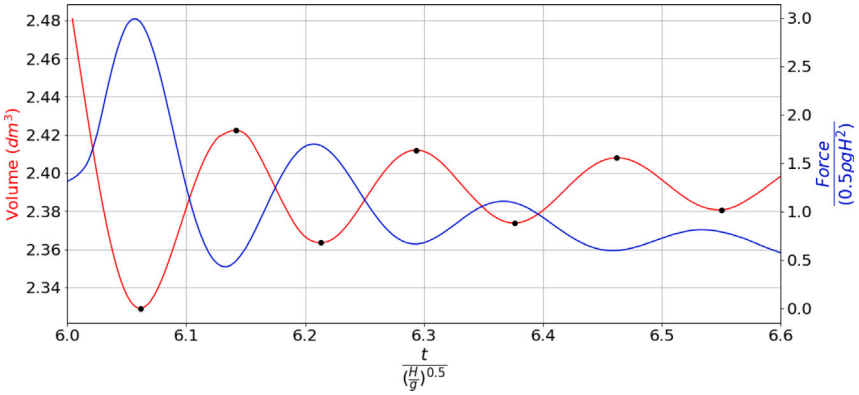

Fig. 12. Time evolution of the impact force F_{wall} (computed by *compressibleInterFoam*-2D, in blue) and the air cavity volume (in red). The black dots indicate the minimum and maximum of the air cavity volume.

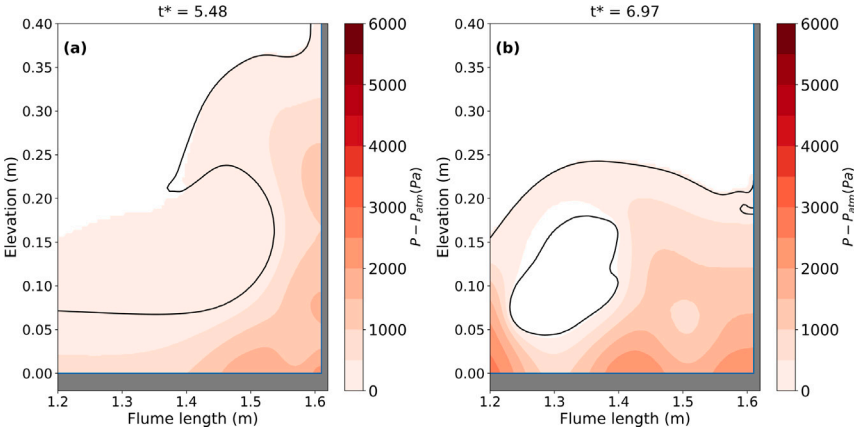

Fig. 13. Pressure distribution near the wall corresponding to $t^* = 5.48$ (a) and $t^* = 6.97$ (b), with $t^* = \frac{t}{\sqrt{H/g}}$.

distribution in the run-up (Fig. 7) with a nil gradient and a very low pressure value on most of the wall, except the bottom.

This pressure distribution is related to the flow characteristics along the wall during this stage of the flow. Considering an inviscid flow and neglecting the horizontal component along the wall, the following equation relating the pressure and the vertical velocity can be written (Ko and Yeh, 2018):

$$\rho\frac{\partial w}{\partial t} + \rho\frac{\partial w^2}{\partial z} + \frac{\partial P}{\partial z} + \rho g = 0 \tag{12}$$

which can also be presented as:

$$-\frac{1}{\rho}\frac{\partial P}{\partial z} = g + \frac{\partial w}{\partial t} + \frac{\partial w^2}{\partial z} \tag{13}$$

This equation shows that the pressure gradient is related to the gravity and the time and spatial evolution of the vertical velocity w. Fig. 15 shows the time evolution of the vertical velocity profile along the wall during the run-up phase. The interesting feature is that, at a given time, apart from the gradient near the bottom, the vertical velocity is constant. This confirms the findings of Ko and Yeh (2018) and Tan et al. (2023), that the run-up flow behaves as a rigid body with constant velocity field at a given time. This also explains why the pressure gradient is nil and the pressure is only atmospheric in most part of the run-up flow. In Eq. (13), the convective acceleration is weak as the velocity is uniform, but the local acceleration is significant due to the variation in time of w in the run-up flow (Fig. 15). The estimation

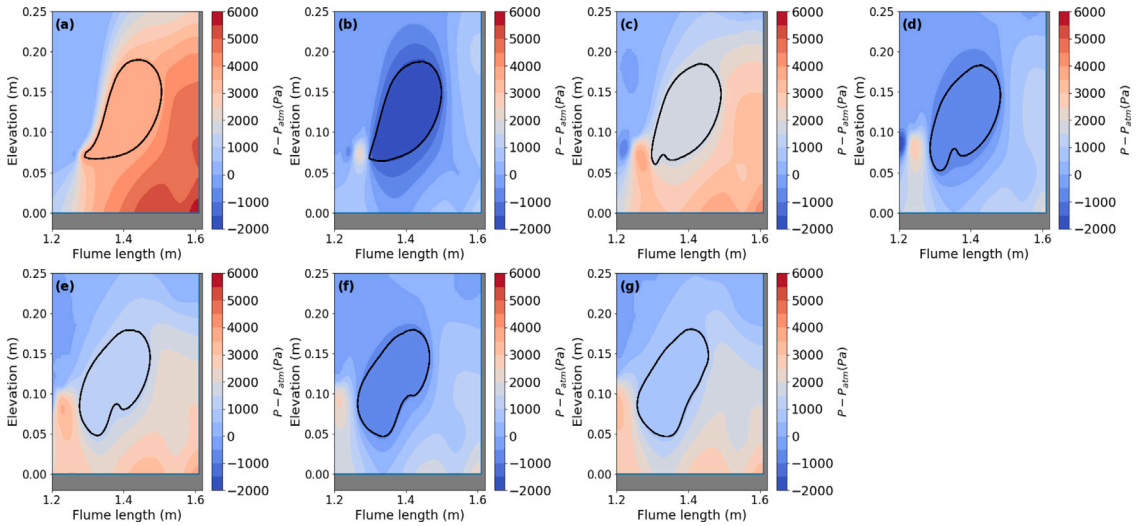

Fig. 14. Pressure distribution surrounding the cavity corresponding to the instants of compression (troughs) and expansion (peaks) of the air cavity volume (also marked by the black dots in Fig. 12).

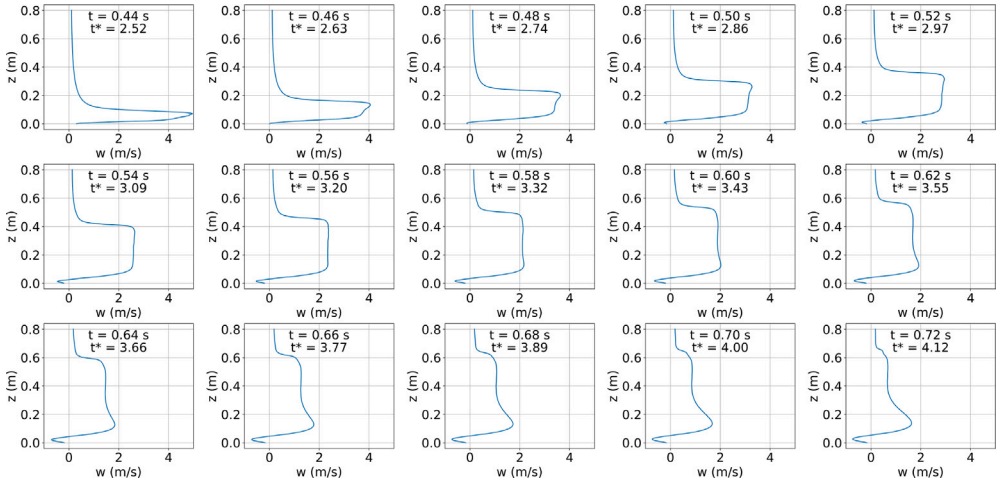

Fig. 15. Evolution with time of the vertical velocity (w) profile along the wall during the surge run-up.

of $\frac{\partial w}{\partial t}$ gives, indeed, values around -10 (ms^{-2}), effectively canceling out the gravity component g, while the term $\frac{\partial w^2}{\partial z}$ is found negligible.

4.2. Pressure and force during the run-down just before the second peak

During the run-down, the situation progressively changes as already analyzed in Section 3.1.4. The time evolution of the vertical velocity profile is shown in Fig. 16. In the upper part of the run-down flow, the velocity is constant until approximately $t^* = 5$, after which, the flow loses its uniformity. This means that the run-up and run-down behave as a rigid body for a large duration. Actually, this part of the flow is in free fall from its initiation to the time when the run-down flow really interacts with the incoming surge, which corresponds to the instant just before the cavity closure (i.e., $t = 1.02$ s).

At this time, the flow can be divided into three zones, each corresponding to a different pressure profile (Fig. 17 panels (b) and (c)). On the lower part of the wall (zone 1), the pressure is controlled by the clockwise recirculation, while the upper part (zone 3) is subjected to the run-down motion. In between (zone 2), the pressure is nearly constant. This constant pressure was also noted in Kihara et al. (2015) (in their Fig. 18).

In zone (1), the pressure variation can be explained with the help of Eq. (13). In this area ($z < 0.1$ m), the flow is quasi-steady as shown in Fig. 16; therefore, the term $\frac{\partial w}{\partial t}$ is negligible. On the contrary, the convective acceleration $\frac{\partial w^2}{\partial z}$ is significant. This term is negative in the upper part of zone (1) then becomes positive toward the bottom. The sum with gravity explains why, in zone (1), when going toward the bottom, the pressure first decreases then increases at a rate higher than the hydrostatic rate.

In zone (3), the problem is more complex as the local acceleration is no longer negligible while the convective acceleration is still important. Interestingly, here the rate of pressure increase is similar to the hydrostatic rate. For that to happen, the convective and local accelerations should cancel, leaving only gravity active. This is indeed what is happening in this area. For instance, at $z = 0.25$ m, the local acceleration is about -10 m s^{-2}, while the convective acceleration $\frac{\partial w^2}{\partial z}$ is positive and of the order of 10 m.s^{-2}.

Let us now explicit the processes at stake in zone (2). The generation of this pressure at this specific time is due to the double deflection of the incoming surge, which is reflected in the opposite direction as part of the reflected jet. The first deflection is due to the wall and the second to the run-down flow.

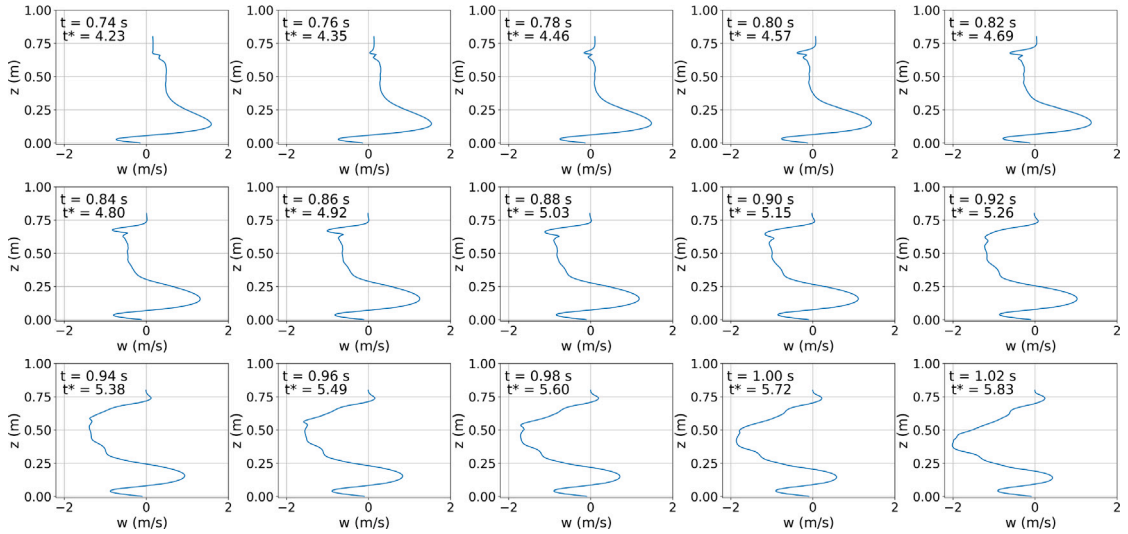

Fig. 16. Time evolution of the vertical velocity (w) profile along the wall during the surge run-down.

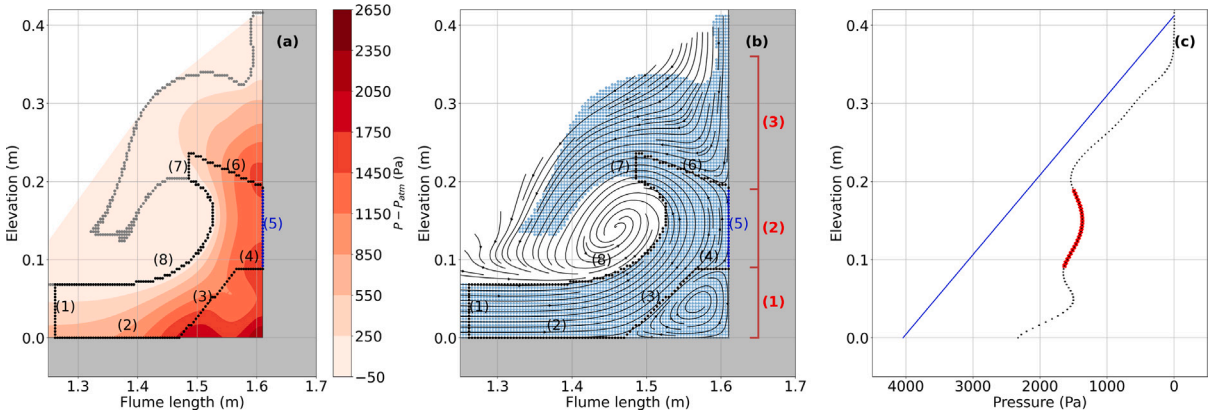

Fig. 17. Pressure field (a), streamlines of velocity (b), control volume boundaries for the momentum conservation theorem (Eq. (14)) (a, b), and pressure profile (c) (at $t = 1.02$ s). On the pressure profile, the blue line features the equivalent hydrostatic pressure distribution corresponding to the water elevation.

Steady jet deflections can be studied with the classical momentum theorem. Here, the control volume is the one represented in Fig. 17(a) and (b). Assuming a steady condition, the momentum theorem reads:

$$\rho\left(\int_{S_1} u^2 dS_1 + \int_{S_7} u^2 dS_7\right) = \left(\int_S P\mathbf{n_{ext}} dS\right)\cdot \mathbf{x} \tag{14}$$

with $\mathbf{n_{ext}}$ being the unit normal vector pointing outward the control volume, S the surface of the control volume and $\mathbf{x}$ the unit horizontal vector. The contribution of the atmospheric pressure overall cancels as it is integrated over a closed control surface. This removes the contribution of S_8, only submitted to $\approx P_{atm}$. S_2 and S_4 are horizontal; therefore, they do not intervene in this equilibrium. The pressure force on S_7 should be very small as the pressure and the surface are small. Finally, the pressure force on S_6 is also not included as the surface is close to the horizontal. Therefore, finally, we may write (as S_3 is approximately 45° inclined):

$$\underbrace{\rho\left(\int_{S_1} u^2\, dS_1\right)}_{150N/m} + \underbrace{\rho\left(\int_{S_7} u^2\, dS_7\right)}_{62N/m} + \underbrace{\int_{S_1} P_1\, dS_1}_{26N/m} \approx \underbrace{\int_{S_3} P_3\, dS_3 \times \cos(45°)}_{104N/m} + \underbrace{F_{def}}_{134N/m} \tag{15}$$

where F_{def} (for deflection) is the force exerted by the flow on the wall in zone (2). The different components of this equation have been evaluated, and the result is indicated under each term. $F_{def} = 134$ N/m can be compared to the integration of the uniform pressure in zone (2), which approximately gives 145 N/m. The equation is only an approximation of the real equilibrium due to the different assumptions considered (error around 7.5%); nevertheless, Eq. (15) illustrates the fact that the uniform pressure in zone (2) is the consequence of the momentum change of the incoming surge fluid particles.

The situation shown in Fig. 17 is the background situation which prevails just before the air cavity closure.

4.3. The effect of the cavity closure

In this section, the influence of the air cavity that superimposes to the contribution of the internal flow structure is discussed. At the time of maximum force (here $t^* \approx 6$), it was observed, with the incompressible 3D model, that the pressure suddenly increases quite uniformly (Fig. 8, panel (c)) and the pressure field deviates from the distribution pattern described in the previous section for a short time. It is also noted, and this is an important observation, that during this phase (i.e., Fig. 8 panels (a2) to (d2)), the flow structure remains identical, which means that this sudden pressure shift cannot be attributed to the flow field in contact with the wall.

With the compressible model, oscillations of the cavity volume in phase opposition with the force on the wall were observed (Fig. 12). Such oscillations were already reported in the case of a direct wave impact on a wall with air entrapment (Bagnold, 1939; Hattori et al.,

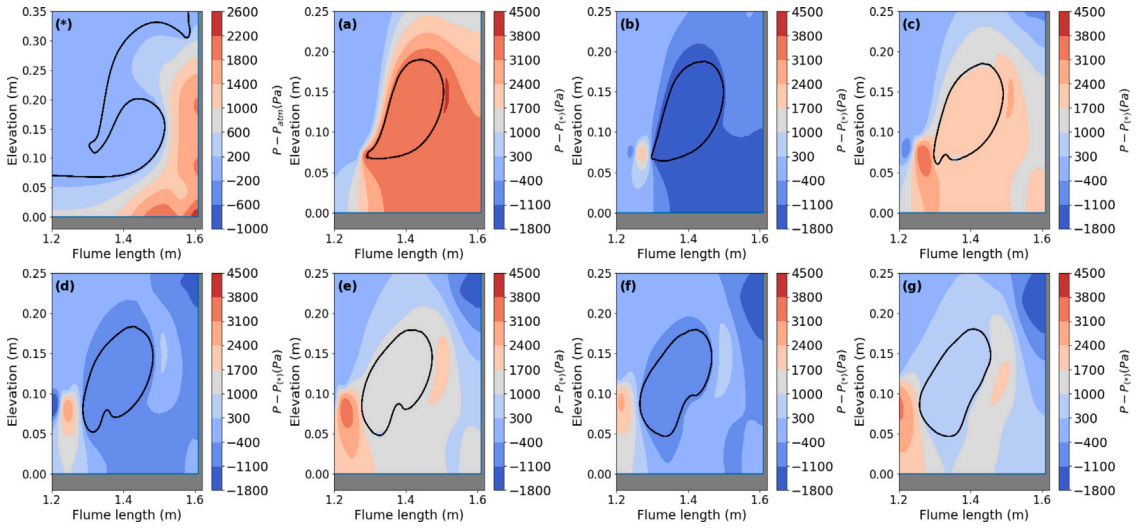

Fig. 18. Distribution of the pressure difference between the instants of Fig. 14 and $t^* = 5.94$ (*) (with $t^* = \frac{t}{\sqrt{H/g}}$).

1994; Lugni et al., 2010a,b; Ma et al., 2016). Bagnold (1939) first understood that the highest pressure shocks measured experimentally were actually due to the compression of small trapped air pockets by a definite amount of the wave momentum, which the author succeeded in determining. A simple piston model was applied to explain this phenomenon.

The process involved in the second peak studied in the present paper may be very similar. Unlike in the Bagnold (1939)'s case, here the air entrapment is not direct and occurs in a second phase during the surge reflection. It is believed that the entrapment has, nevertheless, the same consequence (i.e., a large force generated) due to the confinement of the air pocket between the falling water jet and the two solid boundaries (i.e., the wall and the bottom).

To support this, in the next figure (Fig. 18), an attempt is made to visualize the pressure field only due to the air cavity compression or decompression, by removing the flow contribution on the pressure. For that purpose, the pressure field obtained just before the cavity closure at $t^* = 5.94$ is removed from the instantaneous pressure field computed once the cavity is closed. This assumes that, once the air cavity is closed, its oscillations are very quick and the pressure induced by the flow does not really have time to change during this period. This assumption is supported by Fig. 8 showing that the flow structure does not change significantly between $t^* = 5.71$ and $t^* = 6.06$. It was also verified that the same flow structure is obtained by *interFoam*-3D and *compressibleInterFoam*-2D during this stage.

Fig. 18(a) shows that during the compression of the air cavity, the pressure field in the part of the flow located under the cavity is uniform and close to that calculated inside the cavity. This uniform pressure acts on a large part of the bottom and on the lower part of the wall. It decreases as it rises along the wall and at the bottom upstream of the wall. The same pressure pattern is also observed when the pocket volume is maximum (Fig. 18(b)) but this time with a uniform negative pressure. Subsequently (Fig. 18(c) to (g)), the pressure field has a tendency to become more and more heterogeneous, suggesting a reduction in the influence of oscillation of the cavity volume. However, the effect on the bottom and the wall is still visible.

A uniform maximum pressure inside the air pocket is in line with the piston effect. By continuity, this maximum pressure translates to the water body and compresses the part of water stuck by the domain corner. Upper along the wall, the water particles are less confined, and the pressure decreases. On the bottom, the pressure is high over a larger portion under the action of the pressure due to the cavity compression and the pressure generated at the plunging jet reconnection. This high pressure over a large portion of the bottom is also in line with the measurements carried out by Huo and Liu (2023).

Finally, it is also possible to compare the oscillation frequency of the cavity volume (i.e., $\approx$ 37 Hz), computed with the compressible model, with the analytical estimation of the natural frequency of a two-dimensional bubble given in Topliss et al. (1993). The formula derived in Topliss et al. (1993) in the general case is the following:

$$f^2 = \frac{-2\gamma P\left(1 + \frac{1}{2}\lambda^2 r^2\right)}{4\pi^2 \rho r^2 \left(\log\left(\frac{1}{2}\lambda r \tan(\lambda d)\right) + \frac{1}{4}\lambda^2 r^2\right)} \tag{16}$$

with f is the oscillation frequency, γ the specific heat ratio (set to $\gamma = 1.4$), P the atmospheric pressure, ρ the density of water, r the radius of the trapped air cavity, and d and h the distances from the center of the air cavity to the bottom and the free surface, respectively. The parameter λ is defined as $\lambda = \frac{\pi}{2(d+h)}$. Applying Eq. (16) with our simulation parameters (i.e., $d = 0.11$ m, $h = 0.10$ m, and $r = 0.07$ m, computed from the cavity circumference) results in an oscillation frequency of 36 Hz, which is very close to the value computed by the model.

4.4. The role of air leaks

Fig. 4 showed a large difference between the 2D and 3D incompressible simulations in the shape and, above all, the magnitude of the second peak force. This difference was attributed to the presence of air leaks in the 3D computation at the time of the force peak (Section 3.1.5). Obviously, air leaks reduce the pressure inside the cavity. It is like a piston with a leak; the pressure cannot increase as much as with no leak. In the 2D simulations, there is no air leak, and the pressure increases strongly. In the 3D simulations, air leaks last only over a very short period, which corresponds to the second peak duration or a little bit more ($t^* < 6.04$ in Fig. 4 panel (a)). Then the cavity is closed, and therefore a force peak may be expected. It appears indeed, Fig. 4 panel (a) around $t^* = 6.2$, but it is quite limited because the momentum of the falling water lip is likely no longer sufficient at this time. After this secondary small peak in the 3D simulation, the force gradually decreases. Physically, at this stage, it is likely the flow along the wall which takes over in the contribution of the force. This is supported by Fig. 5, where from this time on, the force corresponds to the hydrostatic component.

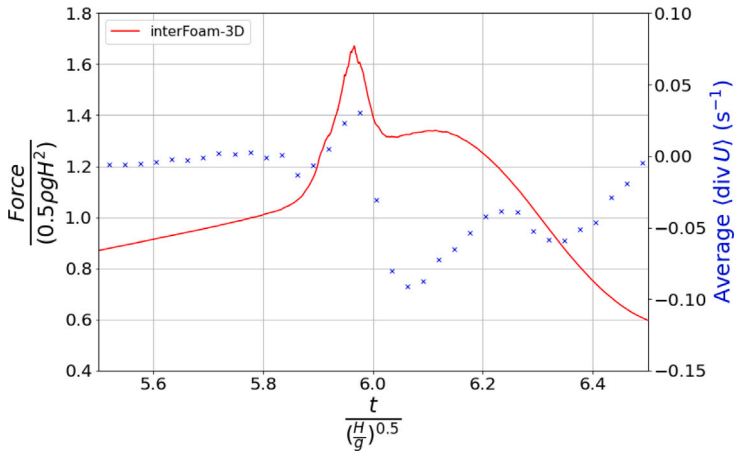

Fig. 19. Evolution of the impact force calculated by *interFoam*-3D and the average velocity-divergence of the air flow around the second force peak.

4.5. Modeling strategy

Our study highlights the ability of the 3D incompressible model to reproduce the overall shape of the force signal generated by both the internal structure of the flow and the formation of an air cavity, unlike the 2D version of the model. As already pointed out, it is believed that this is due to the 3D nature of the flow in the experiment. Indeed, the incompressible code manages to give satisfactory results as long as air can escape relatively easily from the cavity during the closure, which is the case in most 3D cases. This result is all the more interesting as the compressibility of the air necessarily plays a part in this process, as shown by the evolution of the mean divergence computed in the air flow in Fig. 19. Focusing on the reflection phase ($t^* \approx 6$), a significant drop in the divergence is observed, which is synchronized with the maximum force. At this time, the flow is violently compressed in the cavity, and the incompressible model, unable to respond to this constraint, generates artificial compressibility arising from the imperfect resolution of the nil divergence equation (similarly as *interFoam*-2D in Fig. 10). The ability of the air to quickly escape the cavity seems to compensate the violation of the flow incompressibility assumption of the model. However, this modeling strategy fails to account for high-frequency oscillations of the force signal.

It is unlikely that the simulation reproduces perfectly well the experimental flow as the initial conditions of the experiment (i.e. gate velocity, wall roughness, etc.) are not perfectly known. Nevertheless, with comparable air escape, the results in terms of pressure and force appear to be consistent. Therefore, surge impact can be simulated with a 3D incompressible code as long as it is not perfectly 2D, which is the general case.

A 3D compressible simulation could also be an option if the compressible effects are significant. We tried such a simulation for the case studied in this paper and the result in terms of force is plotted in Fig. 20. The force computed with the 3D compressible model is actually very close to the incompressible 3D simulation except for the limited oscillations which appears around $t^* = 6$. It is noted that some oscillations are also present in the measurements but their frequency seems a little bit higher.

4.6. Limitations of the study

Finally, this study has a few limitations which should be stressed hereafter.

The first point concerns the comparison between experiment and simulation. The model and the measurements do not reproduce one unique experiment; they both give an average representation of the experiment (i.e., the RANS simulation is Reynolds averaged, and the measured data is the average over several experiments). Nevertheless, the parameters acting on this average may not exactly be the same. For instance, in the experiment, the gate lifting likely plays an important role which is not simulated, while the RANS model results are dependent on the turbulence model and its parameters. Second, the model convergence was not strictly verified. If explanations were given regarding this matter, nevertheless, due to this, the model results can be considered as subjective. These two points constitute important and interesting scientific questions hidden behind the papers based on the same approach. Nevertheless, at the present time, there is no definitive response to these questions.

This study also focuses on the force on the wall as the reference variable for the reasoning. In the data of Lobovský et al. (2014), there is no direct measurement of the force. In the present paper, the validation of the model was therefore based on an imperfect estimation of the force calculated from the pressure data collected at four points along a vertical profile limited in space. Nevertheless, the topic of this paper is the second force peak for which it was found that the pressure field is rather uniform. So this problem should not jeopardize the main conclusions of the article.

Finally, the surge studied is a particular case corresponding to the study of Lobovský et al. (2014). It is not representative of all the possible surges (with different heights and velocities). It is expected that some results obtained, for instance, regarding the internal structure of the flow, may change with different surge characteristics.

5. Conclusions

In this article, the impact of a surge flow generated with a dry dam break on a wall similar to the experimental measurements of Lobovský et al. (2014) was studied with different numerical models (i.e., incompressible and compressible). The following conclusions can be drawn from this work:

- As expected, all the models predict the appearance of two force peaks. The first one occurs when the surge strikes the wall, the second one when the reflected falling jet collapses onto the incoming flow, creating a cavity with different shapes depending on the model used. All the simulations show that during the occurrence of the first force peak, the pressure field is heterogeneous, while during the second one, it is more uniform.
- The second force peak is computed very differently by 2D and 3D incompressible simulations, the first simulation predicting an unrealistically high peak value, while the second one matches the data much better. The difference is due to the trapping of air in the cavity in 2D, while in 3D, air can partly escape due to a more heterogeneous water free surface. During the closure of the cavity,

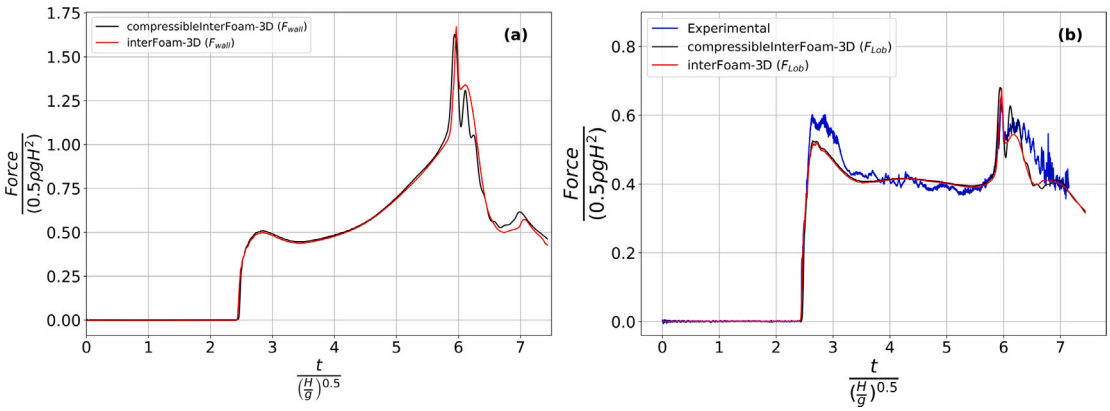

Fig. 20. Evolution of the forces calculated with the *interFoam*-3D and *compressibleInterFoam*-3D. Left panel: F_{wall}, right panel: F_{Lob} and comparison with experimental data.

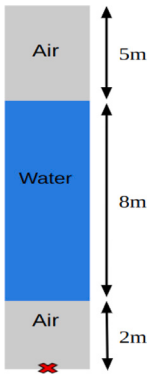

Fig. 21. Sketch of the case studied.

whether in 2D or in 3D, the divergence of the flow becomes negative in this area, witnessing the apparition of compressible effects.

- Before the second force peak, during the run-up motion, the force on the wall is very different from the hydrostatic equivalent force. The pressure is localized in the bottom part of the wall and cancels above this area. This is due to the local acceleration of the run-up flow, which counteracts the gravity. This paper also confirms the rigid body run-up flow assumption first introduced in Ko and Yeh (2018).
- During the run-down motion, there is a strong interaction between the incoming surge flow and the descending run-down flow, which generates the reflected jet. This interaction is associated with an increase of the pressure and the force on the wall.
- Just before the closure of the cavity, the pressure on the wall shows three distinct areas associated with different physical processes. Close to the corner, it is controlled by the clockwise flow recirculation observed in this zone. In the upper part of the wall, the pressure is due to the run-down of the flow. In this zone, the pressure is quasi-hydrostatic. In the middle area on the wall, the pressure is constant. This is the portion of the wall which deflects entirely the incoming jet, hence the different behavior observed. This pattern remains unchanged during the occurrence of the second peak; therefore, this particular flow is not responsible for the second force peak.
- What changes drastically the physics is the closure of the cavity. Here, the 2D compressible simulation shows the appearance of oscillations in the pressure and the force on the wall similar to the ones observed in Bagnold (1939) or Ma et al. (2016) in the case of direct wave impacts with trapped air pockets. As in these works, the cavity volume also oscillates, with the same frequency, but in phase opposition with respect to the force, showing a direct link between the cavity and the force on the wall (i.e., when the cavity is compressed, the force increases, and the other way around).

Finally, this numerical work allowed for a better understanding of the physical processes behind the second force peak in a surge impact. This force peak is due to the compression of the cavity generating a uniform pressure field inside the cavity which, by continuity, and because of the confinement created by the wall and the bottom boundaries, propagates to the water in between and subsequently to the boundaries themselves.

As in Bagnold (1939), the phenomenon is expected to depend significantly on the air pocket size and shape, as well as on the water momentum involved in the falling lip. These two aspects, in turn, should depend on the incoming surge characteristics. Therefore, it appears necessary, as a follow-up of the present work, to investigate this dependency by varying the characteristics of the dam break flow studied.

CRediT authorship contribution statement

Mohamed Rozki: Writing – review & editing, Writing – original draft, Visualization, Validation, Software, Funding acquisition. **Stéphane Abadie:** Writing – review & editing, Writing – original draft, Validation, Supervision, Funding acquisition, Formal analysis, Conceptualization. **Denis Morichon:** Conceptualization, Writing – review & editing, Supervision, Funding acquisition.

Declaration of competing interest

The authors declare that they have no known competing financial interests or personal relationships that could have appeared to influence the work reported in this paper.

Acknowledgments

Mohamed Rozki's PhD grant was funded from the European Union Horizon 2020 research and innovation program under the Marie Curie actions, EDENE, Grant Agreement No. 945416. This research is also carried out under the framework of the joint laboratory KOSTARISK, which is part of the E2S UPPA program managed by the French National Research Agency, France (ANR-16-IDEX-0002) and supported by the French Government's "Investissements d'Avenir" (PIA), France. The joint laboratory KOSTARISK is co-funded by E2S UPPA, the AZTI Foundation and the center Rivages Pro Tech of SUEZ. The authors would finally like to acknowledge the support provided by Hakim Hamdani and Julien Reveillon for the use of *compressibleInterfoam*.

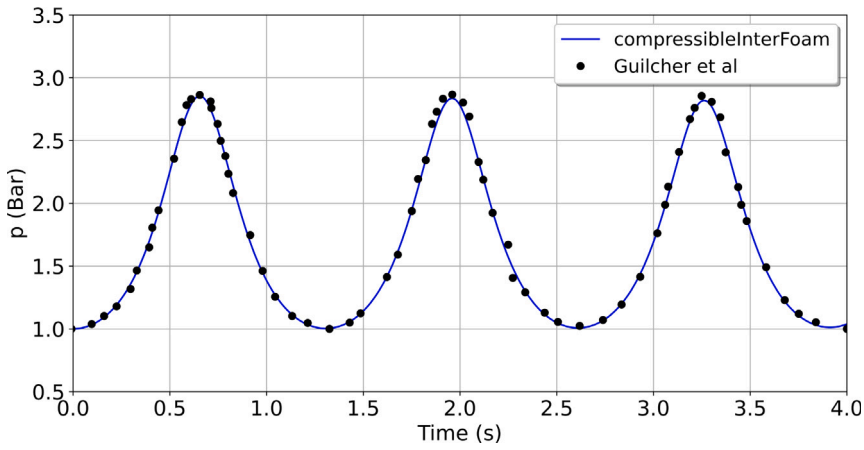

Fig. 22. Evolution of the pressure signal during the compression–expansion cycle of the lower air pocket. This signal corresponds to the red cross probe position in Fig. 21.

Table 2
Setup of the model used to simulate the 1D compression of a gas column.

Guilcher et al. (2010) (Bagnold 1D) *(compressibleInterFoam)*				
Mesh Size	$\Delta x = \Delta z = 2$ m, $\Delta y = 0.005$ m			
CFL	$CFL_{max} = 0.01$ (maxCo)			
Initial conditions	**alpha.water**	**laminar**	**p_rgh** (Pa)	U (m/s)
Initial Values	–	-	10^5	(0 0 0)
Boundary	**alpha.water**	**laminar**	**p_rgh**	U
Walls	zeroGradient		fixedFluxPressure	noSlip

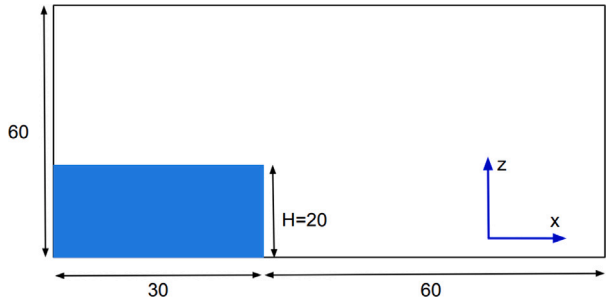

Fig. 23. Sketch of the dam break case studied in Tan et al. (2023). Dimensions are in cm.

Appendix

Validation of compressibleInterFoam -2D in the 1D compression of a gas column

In this section, the compressible model is validated in the case of the one dimensional compression of a gas column by a free falling water column (Fig. 21). This is a standard benchmark test for simulating water–air interactions close to the ideal model proposed by Bagnold (1939). Assuming a perfect gas and an isentropic process, the theoretical formulation of the problem leads to a first order differential equation which can be integrated numerically (Dias, 2008). Guilcher et al. (2010) simulated this case with a two-phase SPH model showing a perfect agreement with the solution of Dias (2008). This benchmark case is also used in Hamdani (2023) to validate *compressibleInterFoam* in a simple configuration avoiding the resolution of the energy equation.

In this section, we compare the results obtained with our implementation of *compressibleInterFoam*-2D, which respect the assumption of the problem, with the results of Guilcher et al. (2010) in the case showed on Fig. 22. In the simulation, the water density is 1000 kg/m^3 and the air density 1 kg/m^3. The initial pressure in air is $p_0 = 10^5$ Pa. The other numerical parameters used for the simulation are indicated in Table 2.

Fig. 22 shows the comparison of the pressure calculated at the bottom of the piston with *compressibleInterFoam*-2D and the model of Guilcher et al. (2010). The match between the two models is very satisfactory.

Validation of interFoam in the case of Tan et al. (2023)

In this section, we reproduce the experiment of Tan et al. (2023) to validate the flow structure calculated by the *interFoam* model (as found in Section 3.1.4). This experiment involves a dam break over a dry bed in a small-scale flume. In this study, a 30 cm long reservoir is filled to a height of 20 cm (Fig. 23). Here, the computation is performed in 3D in order to better match the experiment, which always has some 3D component, nevertheless, the results obtained with a 2D simulation would be very similar. The set-up of the model is provided in Table 3.

In Fig. 24, the water–air interface measured by Tan et al. (2023) is compared to the one calculated by the *interFoam*-3D model at different instants (expressed in non dimensional form $T = t/\sqrt{g/H}$). As in the case of Lobovský et al. (2014) (Fig. 2), the model follows more or less the right trend but fails in reproducing the fine scale 3D features of the flow and especially the water/air mixing inside the cavity.

Fig. 25 shows the velocity distribution and streamlines in the impact zone, calculated by *interFoam*-3D (left) and measured by Tan et al. (2023) (right) with a PIV method. The correspondence is very good at times T = 3.5 and T = 4.55. At T = 5.25, the three zones identified in Fig. 17 in the case of Lobovský et al. (2014), also clearly appears here in the simulation and in the measurement. Overall, the simulation predicts correctly the streamlines and the velocity magnitude at this time, the most important discrepancy being, again, the shape and constitution of the cavity. Finally, at time T = 5.95 corresponding to the closure of the cavity, if some discrepancy can be observed, the main features of the measured flow are present in the simulation.

Data availability

Data will be made available on request.

Table 3
Setup of the model used to simulate the case of Tan et al. (2023).

Tan et al. (2023) *(interFoam)*					
Mesh Size	$\Delta x = \Delta z = 0.002$ m, $\Delta y = 0.005$ m				
CFL	$CFL_{max} = 1$ (maxCo)				
Initial conditions	**alpha.water**	**epsilon** (m^2/s^3)	**k** (m^2/s^2)	**p_rgh** (Pa)	U (m/s)
Initial Values	–	10^{-4}	10^{-4}	0	(0 0 0)
Boundary	**alpha.water**	**epsilon** (m^2/s^3)	**k** (m^2/s^2)	**p_rgh** (Pa)	U (m/s)
Walls	zeroGradient	epsilonWallFunction	kqRWallFunction	fixedFluxPressure	noSlip
Atmosphere	inletOutlet	inletOutlet	inletOutlet	totalPressure	pressureInletOutletVelocity

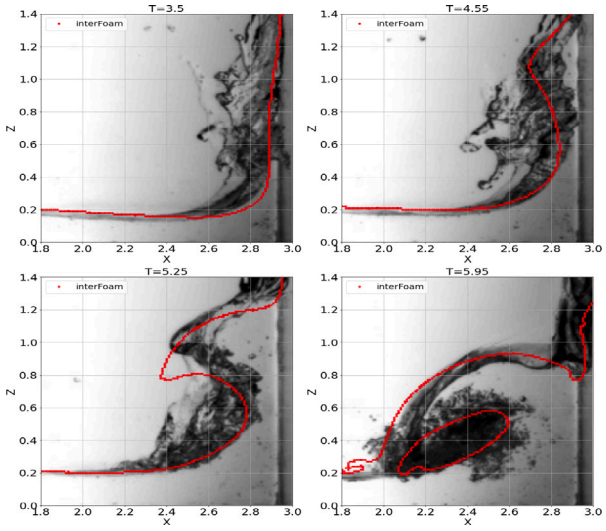

Fig. 24. Comparison of the free surface profiles at four different times from the Tan et al. (2023) experiment (3D view) and the *interFoam*-3D simulation (taken in the central section).

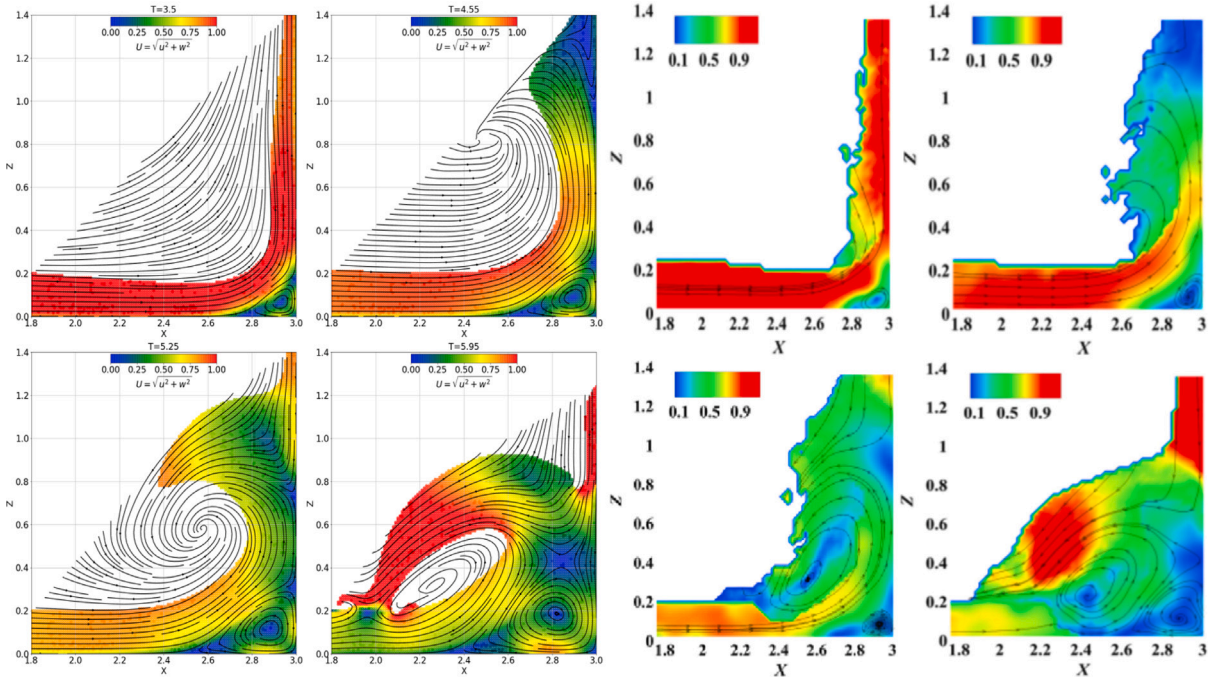

Fig. 25. Velocity magnitude distribution ($U = \sqrt{u^2 + w^2}$) and streamlines calculated by *interFoam*-3D in the central cross section (left) and measured by Tan et al. (2023) (right) in the central section at the same instants.

References

Bagnold, R., 1939. Interim report on wave-pressure research.(Includes plates and photographs). J. Inst. Civ. Eng. 12 (7), 202–226.

Cross, R.H., 1967. Tsunami surge forces. J. Waterw. Harb. Div. 93 (4), 201–231.

Cumberbatch, E., 1960. The impact of a water wedge on a wall. J. Fluid Mech. 7 (3), 353–374.

Deshpande, S.S., Anumolu, L., Trujillo, M.F., 2012. Evaluating the performance of the two-phase flow solver interfoam. Comput. Sci. Discov. 5 (1), 014016.

Dias, F., 2008. Analytical Models for Wave Impact. Technical Report, Gaztransport & Technigas.

Guilcher, P.-M., Oger, G., Jacquin, E., Brosset, L., Grenier, N., Le Touzé, D., 2010. Simulation of liquid impacts with a two-phase parallel SPH model. In: ISOPE International Ocean and Polar Engineering Conference. ISOPE, ISOPE–I.

Hamdani, H.Y., 2023. Caractérisation De L'aération Dans La Modélisation Numérique Des Impacts Liquide/solide (Ph.D. thesis). Normandie Université.

Hattori, M., Arami, A., Yui, T., 1994. Wave impact pressure on vertical walls under breaking waves of various types. Coast. Eng. 22 (1–2), 79–114.

Huo, Z., Liu, H., 2023. Experimental study of the surge-and bore-induced impact pressure on a vertical wall and its foundation. Phys. Fluids 35 (1).

Iphineni, H., Windén, B., Girimaji, S.S., 2024. Toward high-fidelity numerical wave tank development: Scale resolving partially-averaged Navier–Stokes simulations of dam-break flow. Ocean Eng. 291, 116407.

Kankanamge, S.L., Mendis, P., Ngo, T., 2020. Use of fluid structure interaction technique for flash flood impact assessment of structural components. J. Flood Risk Manag. 13 (1), e12581.

Kihara, N., Niida, Y., Takabatake, D., Kaida, H., Shibayama, A., Miyagawa, Y., 2015. Large-scale experiments on tsunami-induced pressure on a vertical tide wall. Coast. Eng. 99, 46–63.

Ko, H.T.S., Yeh, H., 2018. On the splash-up of tsunami bore impact. Coast. Eng. 131, 1–11.

Liu, S., Nistor, I., Mohammadian, A., Azimi, A.H., 2022. Experimental investigation on the impact of dam-break induced surges on a vertical wall. Fluids 7 (8), 258.

Lobovský, L., Botia-Vera, E., Castellana, F., Mas-Soler, J., Souto-Iglesias, A., 2014. Experimental investigation of dynamic pressure loads during dam break. J. Fluids Struct. 48, 407–434.

Lugni, C., Brocchini, M., Faltinsen, O., 2010a. Evolution of the air cavity during a depressurized wave impact. II. The dynamic field. Phys. Fluids 22 (5).

Lugni, C., Miozzi, M., Brocchini, M., Faltinsen, O., 2010b. Evolution of the air cavity during a depressurized wave impact. I. The kinematic flow field. Phys. Fluids 22 (5).

Ma, Z., Causon, D., Qian, L., Mingham, C., Ferrer, P.M., 2016. Numerical investigation of air enclosed wave impacts in a depressurised tank. Ocean Eng. 123, 15–27.

Okagaki, Y., Yonomoto, T., Ishigaki, M., Hirose, Y., 2021. Numerical study on an interface compression method for the volume of fluid approach. fluids 6 (2), 80.

Park, I.-R., Kim, K.-S., Kim, J., Van, S.-H., 2012. Numerical investigation of the effects of turbulence intensity on dam-break flows. Ocean Eng. 42, 176–187.

Ramsden, J.D., 1996. Forces on a vertical wall due to long waves, bores, and dry-bed surges. J. Waterw. Port Coast. Ocean Eng. 122 (3), 134–141.

Shen, J., Wei, L., Wu, D., Liu, H., Huangfu, J., 2020. Spatiotemporal characteristics of the dam-break induced surge pressure on a vertical wall. Coast. Eng. J. 62 (4), 566–581.

Streicher, M., Kortenhaus, A., Gruwez, V., Hofland, B., Chen, X., Hughes, S., Hirt, M., 2018. Prediction of dynamic and quasi-static impacts on vertical sea walls caused by an overtopped bore. In: 36th Conference on Coastal Engineering. ICCE2018, (no. 36).

Streicher, M., Kortenhaus, A., Marinov, K., Hirt, M., Hughes, S., Hofland, B., Scheres, B., Schüttrumpf, H., 2019. Classification of bore patterns induced by storm waves overtopping a dike crest and their impact types on dike mounted vertical walls – a large-scale model study. Coast. Eng. J. 61 (3), 321–339.

Tan, T., Ma, Y., Zhang, J., Niu, X., Chang, K.-A., 2023. Experimental study on flow kinematics of dam-break induced surge impacting onto a vertical wall. Phys. Fluids 35 (2).

Topliss, M., Cooker, M., Peregrine, D., 1993. Pressure oscillations during wave impact on vertical walls. In: Coastal Engineering 1992. pp. 1639–1650.